Astronomy & Astrophysics manuscript no. zgp˙aa September 27, 2005
(DOI: will be inserted by hand later)

Large-Scale Source Regions of Earth-Directed Coronal Mass Ejections

Guiping Zhou, Jingxiu Wang and Jun Zhang

National Astronomical Observatories, Chinese Academy of Sciences, Beijing 100012, China
e-mail: zhougp@ourstar.bao.ac.cn

Submitted May 31, 2005

Abstract. Based on SOHO/MDI, EIT, Yohkoh/SXT, Hα, and other relevant observations, we analyzed all the earth-directed halo coronal mass ejections (CMEs) in the interval from Mar. 1997 to Dec. 2003. A total of 288 earth-directed CMEs were studied and their associated surface activity events identified. Unlike the previous studies that often attributed a surface activity event or given active region to a CME source region, this statistical analysis put emphasis on the large-scale magnetic structures of CMEs, in which the CME-associated surface activity takes place. All the CMEs are found to be associated with large-scale source structures. The identified large-scale structures can be grouped into four different categories: extended bipolar regions (EBRs), transequatorial magnetic loops, transequatorial filaments and their associated magnetic structures, and long filaments along the boundaries of EBRs. The relative percentages of their associated CMEs are 36%, 40%, 13%, and 11%, respectively. The analysis indicates that CMEs are intrinsically associated with source magnetic structures on a large spatial scale.

Key words. Sun: coronal mass ejections (CMEs), Sun: activity, Sun: magnetic field

1. Introduction

Coronal mass ejections (CMEs) often consist of very large structures that contain plasma and magnetic fields that are expelled from the Sun into the heliosphere (Webb, 2000). They are believed to be the main source of strong interplanetary disturbances that may cause intense geomagnetic storms (Gosling, 1997). Since CMEs were first detected in the 1970s, many of their properties have been learned, such as their morphology, geometry, mass, and dynamics (e.g. Hundhausen, 1997; Forbes, 2000). However, some key problems about CME origins are still far from being solved, such as where they initiate or what the characteristics of their source structures are.

Thanks to the joint observations from SOHO (Solar & Heliospheric Observatory, 1996-present; Domingo et al., 1995), MDI (the Michelson Doppler Imager, Scherrer et al., 1995), EIT (the Extreme Ultraviolet Imaging Telescope, Delaboudinière et al., 1995), LASCO (Large Angle and Spectrometric Coronagraph Experiment, Brueckner et al., 1995), Yohkoh SXT (Soft X-ray Telescope, Tsuneta et al., 1991), and the Hα and radio observations, more and more scientists have revealed that CMEs are associated with the commonest near-surface activity events like flares (Shibata et al., 1995; Nitta & Akiyama, 1999; Zhang et al., 2001a), eruptive filaments(Webb & Hundhausen, 1987; Delannée, Delaboudinière & Lamy, 2000; Zhang, Wang & Nitta, 2001b; Subramanian & Dere, 2001), moving magnetic features (e.g. Vrabec, 1971; Lee, 1992; Zhang & Wang, 2002), magnetic flux emergence (e.g. Feynman & Martin, 1995; Wang & Sheeley, 1999; Chen et al., 2000), and magnetic flux cancellations (e.g. Martin, 1986; Wang & Shi, 1993; Zhang et al., 2001c).

More recently, Zhou, Wang, and Cao (2003) identified closer correlations between CMEs and surface magnetic activity with a sample of 197 earth-directed CMEs. These studies provided clues about the CME triggering processes. However, as a kind of large-scale solar activity, CMEs are very disproportional to these surface activity events being observed on such a small scale. As an example, when a CME was associated with a flare, it seemed that the related flare only appeared in an active region (AR). However, most of the time, larger volume changes around the AR were observed in the corona. This indicates, therefore, that each CME may have a corresponding source magnetic structure that has an intrinsically large spatial scale.

Statistics and case studies also provide hints about CME-associated large-scale magnetic structures. X-ray or EUV dimmings (brightness depletions) are expected to be the very first signature of CMEs, often originating from ARs and extending to large areas most of the time (Rust & Hildner, 1976; Sterling & Hudson, 1997; Gopalswamy & Hanaoka, 1998; Thompson et al., 2000). CMEs are sometimes observed arising from a coronal streamer, a preexisting large-scale structure (e.g. Hundhausen, 1993; Subramanian, 1999). AR-interconnecting or transequatorial loops observed in SXR or EUV that link the primary flaring site and other magnetic regions are related to

Send offprint requests to: Guiping Zhou

CMEs (Klimchuk et al., 1994; Khan & Hudson, 2000; Chertok, 2001; Harra et al., 2003; Cheng et al., 2005). A transequatorial filament and its related large-scale magnetic field is also recognized as being closely linked to CMEs (Wang, 2002b, Wang, et al., 2005a, b). They suggest that a long eruptive prominence and its overlying coronal cavity, as well as the ambient corona, are the pre-event structures that erupt to become a three-component CME (Webb, 2000). Thus, CMEs seem to involve both the smaller scale activity and this destabilization of large-scale coronal structures. Since the most commonly associated activity on a small scale are very likely not the main driving force for CMEs (e.g. Hundhausen, 1999; Lin, 2004), it becomes important to understand the CME origins from the configuration and evolution of rather large-scale magnetic structures.

As suggested by Zirin (1985), there might be a hierarchy to solar activity. From tiny mini-filament eruption (Wang et al., 2000) on the quiet Sun to flares in ARs, to global CMEs, activity takes place on a small-scale, on AR scale, and on a large or global scale, respectively. Each level of activity is proposed as the manifestation of magnetic structures destabilizing on the corresponding scale (Wang, 2002b). For example, flares or AR filaments seem to be specified by the sunspot fields on AR scale. So it is suggested that each CME may have a corresponding source magnetic structure with an obviously large spatial scale. Moreover, those large-scale magnetic structures that host CMEs may appear to be an intrinsic component of solar magnetism. Their destabilization, expansion, and eruption into interplanetary space are the basic processes that lead to CMEs.

To understand CME initiation and onset mechanisms, the characteristic magnetic evolution of large-scale magnetic structures should be studied or else meaningful results can never be obtained in the studies of the CME mechanism (Wang et al., 2002c). However, there have so far been no systematic efforts to investigate the large-scale source structures of CMEs.

The current study attempts to determine whether or not we can identify either some typical large-scale magnetic structures or patterns that may be considered as the pre-eruption magnetic topology or parent magnetic structures of CMEs. To make the study useful for CME prediction, we chose the primary data base as the commonly-accessible MDI synoptic charts, in which large-scale magnetic structures can be adequately revealed, and selected the full disc EIT and the soft X-ray and Hα intensity structures as necessary supplements. Our purpose was to identify a few types of large-scale structures in photospheric magnetic fields that are closely correlated with the initiation and development of CMEs. The basic logic is to first allocate the CME-associated activity events, say filament eruptions, flares, and/or relevant ARs, in the MDI magnetic synoptic charts, then to extract the common features of these CME-prolific large-scale magnetic structures, and finally to develop the necessary statistics on the different levels of CME productivity for each type of large-scale magnetic structures.

The data analysis is presented in the next section, while Sect. 3 describes the categories of the large-scale source magnetic structures of CMEs. Section 4 presents the statistics, and the conclusion and discussion are given in the last section.

2. Data analysis

The successful missions of SOHO and Yohkoh made disc observations possible, particularly for earth-directed CME initiations. To avoid ambiguity in locating CME-associated surface activity, as discussed by Feyman & Martin (1995), only earth-directed halo CMEs were selected in our statistics. A CME with span angle greater than 130^0 is referred to as a halo CME in our approach.

CMEs were selected from the catalog on the website of http://cdaw.gsfc.nasa.gov/CME list/ in the interval from Mar. 1997 to Dec. 2003, as observed by LASCO aboard SOHO. To clearly identify the earth-directed halo CMEs and to study their large-scale source regions, many other space-borne and ground-based observations were analyzed. We explored the observations from the instruments EIT, LASCO, and MDI on SOHO. In addition, Yohkoh SXT images were necessary, as well as Hα filtergrams, which come from Big Bear Solar Observatory (BBSO), Huairou Solar Observing Station (HSOS), Hiraiso Solar Terrestral Research Center (HSTRC), and Holloman Air Force Base (HAFB).

Two criteria for identifying these earth-directed halo CMEs are discussed in the paper by Zhou et al. (2003). One is that the associated surface activity appeared in the time interval *(CME initiation time ± 30 min)*. Here the *CME initiation time* means the approximate time of CME initiation from the solar surface. It was obtained by inverse extrapolation of the CME front from 2.2~30 $R_\odot$ to 1 $R_\odot$ according to a linear fitting of height-time curves based on LASCO C2/C3 observations. Most CME initiation times were taken from SOHO LASCO CME Category (see http://cdaw.gsfc.nasa.gov/CME list/), and a small number of them were extrapolated by the authors. The other criterion was that the surface activity's position identified in the EIT images was under the span of the associated CME or just near the span edge. If both criteria were satisfied, the CME was considered to be Earth-directed. A total of 288 earth-directed halo CMEs from Mar. 1997 to Dec. 2003 were identified well.

This database provided nearly complete temporal coverage of the observations. The MDI synoptic charts in particular provide a good opportunity for studying large-scale source regions of CMEs. Most CMEs, whatever their associated surface activity, are initiated within some type of large-scale, well-organized, magnetic field regions (Hundhausen, 1988). To explore the properties of large-scale magnetic structures, the positions of CME-associated surface activity in EIT observations were allocated to the corresponding MDI synoptic charts. As shown in Fig. 1, a CME-associated flare on April 26, 2001 was identified from an EIT image (see the black arrow), with its central location (N23W05) considered as the CME initiation site. This initiation site was further allocated on the corresponding MDI synoptic chart (asterisk in the left panel). Then, we investigated the large-scale source structures of all the 288 earth-directed CMEs by combining the MDI synoptic charts with the other SXR, EUV, and Hα observations.

From the MDI synoptic charts, it was found that the CME initiation sites are often located in some large-scale magnetic structures that present regular magnetic morphologies in the photosphere. One of them is of particular interest: coherent

large-scale bipolar flux region. By coherent we mean that the large-scale magnetic bipoles follow the Hale polarity law for ARs in each solar cycle and also change their magnetic orientations from one cycle to another cycle. It is natural to call these large-scale magnetic structures *extended bipolar* regions (EBRs) (see the right panel of Fig. 1). In the 23rd Solar Cycle, the leading polarity of an EBR in the northern hemisphere is positive, while negative in the southern hemisphere.

The size of an EBR in this study falls in the range of 34° ~ 197° in longitude and of 33° ~ 83° in latitude. As an entity, an EBR region involves flares, ARs and quiescent filaments, magnetic flux eruption, and magnetic shearing (Feynman & Hundhausen, 1994; Feynman, 1997). All these surface activity events are observed to be possibly associated with CMEs. Although it is not known exactly whether EBRs are the parent magnetic structures of CMEs, many CMEs have been found to close correlate with EBRs. Therefore, they are considered as a form of large-scale magnetic field structure that is associated with CME initiation. In order to show the large-scale background magnetic structures more clearly, we sometimes smoothed the MDI synoptic data over 10~20 pixels.

3. Categories of CME large-scale source structures

Based on the combined analysis of MDI magnetic field data and other multiple-wavelength observations, the large-scale source structures of CMEs were classified into four different categories (see Fig. 2): Category One (C1), EBRs (top row); Category Two (C2), transequatorial magnetic loops (the second row); Category Three (C3), transequatorial filaments and their associated magnetic fields (the third row); and Category Four (C4), long filaments along the boundary of EBRs (bottom row). The asterisks in the figure indicate the CME initiation sites in MDI synoptic charts.

3.1. Category One, EBRs

After allocating the CME initiation sites in the corresponding MDI synoptic charts, we found that a large fraction of them are situated in EBRs. There are two kinds of association between CMEs and magnetic activity that appear inside EBRs as indicated in the top two panels of Fig. 2. One is that CMEs are associated with long filament eruptions above the magnetic neutral lines (polarity inversion lines) of the EBR, which we will call as C1(a). The eruptive filaments can be identified from both EIT images and Hα filtergrams. They often have same lengths as the EBR neutral lines (see the black line in the top left panel of Fig. 2). The other C1(b) is that CMEs are related to AR activity in EBRs (top right panel of Fig. 2). The AR activity events include flares, AR filament eruptions, magnetic surges, and possible magnetic flux changes. There are 104 CMEs whose source structures were identified as EBRs. Two examples are demonstrated to explain the two kinds of associations in this category.

The first example is a CME that occurred on Oct. 25 1999 associated with a filament eruption in an EBR. The leading edge of the halo CME first appeared southward at 14:06 UT in the field of view of LASCO C2 (see Fig. 3A). The associated filament eruption began at 13:36 UT. The post-flare loops that formed after its eruption are shown in EIT images (arrow in Fig. 3B). The filament in its pre-eruption stage can be observed clearly in an Hα filtergram (Fig. 3C). By allocating the CME associated surface activity in the corresponding MDI synoptic chart in Carrington Rotation (CR) 1955 (Fig. 3D), it can be seen that the Hα filament is at the site of an EBR neutral line in the southern hemisphere. The quadrangles in Figs. 3C and 3D outline the same filament in the Hα image and the MDI synoptic chart, respectively. With the same identifying method, 41 CMEs are found to relate to long eruptive filaments above the magnetic neutral lines of EBRs.

The remaining 63 CMEs in this category were recognized to be associated with AR activity in EBRs. The associated ARs were in the close vicinity of the EBR neutral lines. Figure 4 shows the second example that belongs to this kind of CME. A CME on July 26, 2002 first appeared at 22:06 UT in the field of view of LASCO C2 and continuously spread southeastward (see Fig. 4A). Its associated flare started at about 21:00 UT in the position of S22E22 according to EIT observations (e.g., Fig. 4B). There were AR filaments (see Fig. 4C) erupting in the AR that accompanied the flare activity. After locating the CME-associated AR activity in the MDI synoptic chart in CR 1992, we found that the relevant AR was located in an EBR, a coherent large-scale magnetic structure as shown in Fig. 4D. The EBR is illustrated even more clearly by artificially weakening its surrounding magnetic features. A dash in Fig. 4D indicates the EBR neutral line, near which the associated AR lies.

In total, there are 104 CMEs initiated in EBRs, which themselves constitute 36% of all the 288 earth-directed halo CMEs.

3.2. Category Two: transequatorial magnetic loops

The second category discerned for CME-associated large-scale structures is comprised of transequatorial magnetic loops, evidence of which was first observed in Skylab X-ray data (e.g., Chase et al., 1976; Svestka et al., 1977; Pevtsov, 2000). They may develop between existing ARs or between a mature region and new magnetic flux shortly after flux emergence. Approximately one-third of all ARs on the Sun exhibit transequatorial loops (Pevtsov, 2000). Harra et al. (2003) discovered flare behavior of transequatorial magnetic loops. As shown in the second row of Fig. 2, the CME-associated transequatorial loops observed in EIT or SXT images are overlaid in the corresponding MDI synoptic charts. They are represented by solid lines, and they stride the opposite solar hemispheres. During the erupting process of CME-associated surface activity, the plasma within the loop forms part of the CME material.

Figure 5 presents a CME on Nov. 5, 1998 where its large-scale source structure is recognized as a transequatorial loop. From the LASCO C2 observations (see Fig. 5A), we find that the CME propagated northwest from its first appearance at 20:44 UT. Its associated surface activity, a GOES M8.4 flare, began at 19:00 UT in the position of N22W18 identified from the EIT image (black arrow in Fig. 5B). The flare is spatially and temporally associated with transequatorial loops in Fig.

5B. The X-ray analog of the transequatorial loops is also seen in the SXT image (arrow in Fig. 5C). Figure 5D shows the flare and the transequatorial loop in the corresponding MDI synoptic chart in CR 1942. The transequatorial loops connect a complex AR in the northern hemisphere with a plage region in the southern hemisphere. All together, they constitute a large-scale source structure of the CME.

In order to get some idea of the height of the identified transequatorial loops observed from EIT or SXT images, we selected an associated transequatorial loop on Nov. 6 1997, where the distance between the two footpoints is very long, as an example. It was assumed that the distance between two footpoints of a transequatorial loop was directly proportional to its height. We calculated the loop's height following Loughhead, Wang, and Blows (1983). This method is based on the assumptions that (1) the loop's central axis lies in a plane, (2) its footpoints can be located, and (3) it is symmetrical in its own plane about an axis at right angles to the line joining the footpoints. As a result, we get the loop's height of 4.2×10^5 km. For this example, the distance between two footpoints of the observed X-ray loop is 6.4×10^5 km in heliographic coordinates, and its height is 2/3 of its footpoint distance. It would be quite safe to assume that the height of a transequatorial loop is 0.5 - 1.0 times of its footpoint distance by considering the different shapes of the loops. Since the distance between the footpoints of this transequatorial loop was almost the longest one in our sample, we estimated that the height range of the transequatorial loops identified in our work, which can be observed from EIT or SXT images, may not be more than 5.0×10^5 km. However, using the extrapolation method of a potential magnetic field (Wang, et al., 2002a), it is found that part of the associated transequatorial magnetic lines was higher than 1.0 $R_\odot$, i.e., 7×10^5 km. Therefore, it cannot be excluded that some associated transequatorial loops might be even higher than 5×10^5 km in the corona, outside of the field of view of observations. In addition, some transequatorial loops may lack necessary SXR data. Under these conditions, they may not be easily identified from EIT or SXT observations.

Alternatively, dimmings are sometimes associated with large transequatorial loops (Maia et al., 1999; Wills-Davey & Thompson, 1999). The observed dimmings are due to a decrease in plasma density during the opening of the transequatorial loops (Delann*é*e & Aulanier, 1999, Harra & Sterling, 2003), so the transequatorial dimmings can be considered as the proxies of transequatorial loop-like structures. Dimmings can be observed well in EUV (Dere et al., 1997; Bumba, Garcia & Jordan, 1998; Gopalswamy et al., 1998; Thompson et al., 1998; Delann*é*e, Delaboudinière & Lamy, 2000). Thus by using those EIT data that have full coverage for all the 288 earth-directed CMEs, transequatorial dimmings are identified as the manifestation of associated transequatorial loops from EIT base-difference or running-difference images for some events. As indicated in Fig. 6, the associated surface activity of a CME on Nov. 24 2000 is an X-ray flare of X2.3 class (see the arrow in Fig. 6A). Since we could not find an SXT image before 05:12 UT on Nov. 24, a SXT image at 09:18 UT on Nov. 23 was presented. From the EIT or SXT images (see Figs. 6A, 6B), we could not easily observe the associated transequatorial loop connecting AR 9236 with a region in the southern hemisphere. However, there was transequatorial dimming across the two solar hemispheres (Panel C). In this case, we consider that the CME is related to transequatorial loops. Moreover, using the extrapolation method of potential magnetic field (Wang, et al., 2002a), a bundle of transequatorial magnetic lines were found to exist above the transequatorial dimming (arrow in Panel D). These magnetic lines may be considered as the associated transequatorial loops.

As a result, 116 CMEs, whose source structures were associated with transequatorial magnetic loops in SXT or EIT observations, were identified in Category C2. They constitute up to 40% of all the 288 earth-directed CMEs. In most cases, the individual flux systems tend to have the same helicity sign or chirality (Wang et al., 2004). As suggested by Canfield et al (1996) and Pevtsov (2000), only the interconnected regions with the same helicity sign can form transequatorial loops. That is to say, the transequatorial loops, together with the interconnected regions, have the same helicity sign in their magnetic field and represent at least a part or all of a large-scale intercoupled magnetic flux system.

However, as a rule for hemispheres (Seehafer, 1990; Pevtsov et al., 1995, 2001; Abramenko, 1996; Bao & Zhang, 1998), magnetic flux regions on the two solar hemispheres generally have opposite signs of helicity. A transequatorial loop has the same helicity sign, but connects magnetic flux regions that are located on the opposite hemispheres, which implies that one foot of the transequatorial loop should be surrounded by magnetic flux with opposite sign helicity. Wang et al. (2004) suggested that the interaction and reconnection of flux systems with opposite sign helicity are key elements in the magnetism of CME initiation. This might be the reason so many CMEs are associated with transequatorial loops, which appear to be the favorite pre-CME large-scale source structures. This revelation may be useful for CME predictions.

3.3. Category three: transequatorial filaments & their associated magnetic fields

Filament eruptions, one of the earliest known forms of mass ejections from the Sun, are the near-surface activities that are most frequently associated with CMEs, and they have received considerable attention since the late 1900s (Webb, Krieger & Rust, 1976; Munro et al., 1979; Webb & Hundhausen, 1987; St Cyr & Webb, 1991; Tandberg-Hanssen, 1995; Zhang & Wang, 2000; Gopalswamy, 2003). They can erupt on different scales, from mini-filaments to AR filaments to long eruptive filaments. Since sometimes long filament eruptions themselves can reach the scale of a CME, we consider these filaments and their associated magnetic fields as probable large-scale source structures of CMEs. The length of the long eruptive filaments considered are at least greater than 300 arcsec, and the longest of them can reach 1900 arcsec. Except for some long eruptive filaments located in EBRs, the associated long filaments are further grouped into transequatorial filaments (C3) and long filaments along the boundaries of EBRs (C4), which are thought

of as two forms of CME large-scale source structures. Wang (2002b) used the term of giant filament and filament channel to describe this type of CME parent magnetic structure.

One example that illustrates the CMEs correlated with eruptive transequatorial filaments is presented. Wang and his co-authors first recognized the role of transequatorial filaments in the initiations of CMEs (Wang, 2002b, Wang et al., 2005a, b). As indicated in Fig. 7, a CME-associated eruptive transequatorial filament began to elongate and twist from 11:00 UT on Sep. 12, 2000, accompanied by an M1.0 flare in X-ray importance. At 11:54 UT, the corresponding CME first appeared in the field of view of LASCO C2 and expanded southwest (see Fig. 7A). After the filament eruption, post-flare loops formed in EIT observations (see the arrow in Fig. 7B). Since there were no clear Hα observations to show the morphology of the pre-erupting filament, an Hα image after the filament eruption is given as Fig. 7C. The eruptive transequatorial filament is identified in the MDI synoptic chart in CR 1967 of Fig. 7D. The filament lies along the boundary of a transequatorial background magnetic flux with the same polarity. In fact, for the large-scale magnetic structures of the CMEs in C3, we could always see that the enhanced magnetic flux of the same polarity concentrated in the lower latitudes in MDI synoptic charts, which go through the opposite hemispheres on the Sun. This is the common property of the background magnetic morphology for transequatorial filaments.

Just like transequatorial loops, since transequatorial filaments go through the opposite hemispheres with different vorticity and helicity properties, it is speculated that transequatorial filaments and their magnetic arcades would also be unstable. But unlike the transequatorial loops, a transequatorial filament and its magnetic arcades seem to present a large-scale magnetic shear in the solar atmosphere. Their associated CMEs are suspected having some distinct properties, which will be studied in our next work.

A total of 37 CMEs were identified as being associated with transequatorial filament eruptions in this category that includes 13% of all the CMEs.

3.4. Category Four: filaments along the boundaries of EBRs

In addition to the related eruptive transequatorial filaments, long eruptive filaments along the boundaries of EBRs and their related magnetic fields are classified as the fourth category of CME large-scale source structures. This group can exist along the boundary between two/three EBRs or can separate the polar coronal holes from the medium to high latitude EBRs. In the latter case, the filaments act as polar crown filaments (McIntosh, 1980). CMEs associated with these filaments were studied by Zhou et al. (2005).

An example is given to show this category. A CME on Jun. 5, 1998 was related to the eruption of a filament along the boundary of three EBRs. The CME first appeared at 7:02 UT during LASCO C2 observations. The associated eruptive filament began to erupt at 04:39 UT in EIT observations. Figure 8B presents post-flare loops after the filament eruption. An Hα image on June 4, 1998 shows the filament before its eruption (in Fig. 8C). The eruptive Hα filament is further mapped in the corresponding MDI synoptic charts in CR 1936 and 1937 (black line in Fig. 8D). It was located along the boundary of three EBRs. In order to show the associated EBRs more clearly, a procedure was used to make the other magnetic features weak, smoothing the MDI synoptic data over 10 pixels and displaying it in a restricted range. There are 31 CMEs (11%) whose related large-scale source structures were grouped into C4.

Table 1. Categories of CME large-scale source structures

Associa. large-scale source structures	CME number	percent
C1, EBRs	104	36%
C2, transequatorial magnetic loops	116	40%
C3, transequatorial filaments	37	13%
C4, filaments along the boundaries of EBRs	31	11%
Total earth-directed CMEs	288	100%

Table 2. Associations of CMEs with ARs and long eruptive filaments

Associations	CME number	percent
related to ARs	231	80%
related to long eruptive filaments	109	38%
Total earth-directed CMEs	288	100%

4. Statistics

Using the observations from the SOHO LASCO, EIT, MDI synoptic & daily magnetograms, Yohkoh SXR, GOES X-ray, and Hα observations, we extended the CME sample used in Zhou et al. (2003) to 288 earth-directed halo CMEs from Mar. 1997 to Dec. 2003, including the rising and the declining phases of Solar Cycle 23. We present the first systematic study of large-scale source magnetic structures of earth-directed halo CMEs. Detailed information for each CME is appended in Table A1, where we list the CME category according to the large-scale source structure, date, first time seen in LASCO C2 observations (TM), central position angle (CPA), span angle (Width), linear fit speed (Speed), position of associated surface activity on the solar surface (Position), and the NOAA number of related ARs. If a CME is correlated with more than one AR, we only give one of the NOAA numbers of the CME-associated ARs.

As a result, the identified large-scale source structures of all the 288 CMEs are classified into four groups: (C1) EBRs, (C2) transequatorial magnetic loops, (C3) transequatorial filaments and their associated background magnetic structures, (C4) long filaments along the boundaries of EBRs. Among them, the EBRs and the transequatorial magnetic loops are significantly CME-prolific. The associated CMEs constitute 36% and 40% of all the earth-directed CMEs. Though the other two identified large-scale source structures are only related to a small fraction of CMEs, they present some distinguished characteristics that are favorable to the occurrence of CMEs. The different levels of CME productivity for each class of large-scale magnetic structures is summarized in Table 1.

Another statistic about the associations between CMEs and ARs and long eruptive filaments is listed in Table 2. Regardless of the background magnetic fields of associated surface activity, about 38% CMEs are related to long filament eruptions. This means that the instabilities of long filaments correlate closely with CMEs. For the relationship between ARs and CMEs, about 80% CMEs are related to ARs, which is similar to results in Zhou et al. (2003).

The statistics presented in this paper follow a rule that when a CME was related to more than one type of large-scale magnetic structure, we always chose the structure which appeared more specific or characteristic as the CME source structure. For example, if a CME-associated surface activity happened in an EBR and, at the same time, took place in association with transequatorial magnetic loops, we selected the transequatorial magnetic loops as the large-scale source structure of the given CME. The reason is that transequatorial loops are more specific, and they represent a larger magnetic flux system, which an EBR cannot fully cover.

Although the identity of the large-scale source magnetic structures of CMEs is based on detailed analysis of a combined data set, several key factors still exist that may bring uncertainties into the statistics. First, for some CMEs, especially those initiated close to the solar limb, their associated surface activity may be misidentified. They may even be Earth-away CMEs. The lack of coronal observations in the range of 1.0∽2.2 $R_\odot$ severely constrained us from directly imaging the early development of CMEs, while the low cadence of LASCO and EIT observations would not allow us to accurately determine the time of CME initiation or the associated surface activity (Zhou et al., 2003). We estimated that all the above inaccuracy may be less than 5% of the total 288 CMEs. Secondly, the identity of transequatorial loops may not be accurate in the following situations: (1) when the related transequatorial loops are located at the limb of the Sun, they suffer from heavy projection effects; (2) if heated to higher temperatures or situated in the higher corona, they may be put out of the range ($\leq 5\times10^5$ km) of EIT or SXT observations; and (3) on the other hand, some resemblant or fuzzy structures in EIT or SXT observations may be mistaken for transequatorial loops. Since we confirm the associated transequatorial loops by direct observations of EIT and SXT images where possible, together with the observable transequatorial dimming and potential extrapolation of 3-dimension magnetic lines of force, the ambiguity could be minimized. The fact that the data base covers almost 7 years and a large sample makes the statistics meaningful.

5. Discussion and conclusion

The large-scale source structures are identified and classified into four groups (C1)-(C4) for the 288 earth-directed halo CMEs: (C1) extended bipole regions (EBRs), (C2) transequatorial magnetic loops, (C3) transequatorial filaments and their associated background magnetic structures, and (C4) long filaments along the boundaries of EBRs. The associated CMEs in each category constitute 36%, 40%, 13%, and 11% of all the 288 earth-directed CMEs, respectively. These four categories present the large-scale characteristics of CME source magnetic structures. In addition, if only considering the long eruptive filaments from the four categories, 38% of the CMEs are related to long filament eruptions. It presents a close relationship between CMEs and long eruptive filaments (Wang, 2002b). We also look at the relation between CMEs and ARs. AR fields have a smaller scale than the large-scale source regions described in this paper, but they show great magnetic complexity with strong magnetic intensity. They may interact with larger scale structures and possibly lead to the instabilities of large-scale magnetic structures through magnetic emergence and/or cancellation. Similar to the result of Zhou et al. (2003), approximately 80% of the CMEs are related to ARs in the enlarged sample. The identity of favorable large-scale magnetic structures supplemented with detailed vector field observations in relevant ARs may make the CME predictions possible in the future.

In Zhou et al. (2003), we illustrated the close correlations between CMEs and solar surface activity. All the CMEs are accompanied by some solar surface activity in the form of either flares, or filament eruptions, or both. However, the associated magnetic evolution, say in an AR, normally presented no difference among flares with and without CMEs. All of the eruptive activity events, e.g., flares and filament eruptions, are driven by the rather similar process observed in the photosphere, which was interpreted by Song et al. (2002) as the transport of magnetic energy and complexity into the higher solar atmosphere. We speculated that the associated surface activity may act as either triggers of the instability of the globally-coupled magnetic flux systems with different spacial scales, or the local manifestation of the instability, while the real basis for deciding CME properties should be the pre-CME large-scale source structures. Though some studies about the large-scale magnetic activity associated with CMEs have already been carried out, the analysis in this paper is the first attempt to investigate the large-scale source structures of CMEs based on the MDI magnetic synoptic charts.

This is only the first step in our series of studies to identify and classify the large-scale magnetic structures that favor CMEs. Work needs to be done to evaluate the reliability and feasibility of the categories. Further, for example, we need to know the topological connectivity of the 3-D magnetic lines of force for each kind of large-scale source structure, and whether we can use their properties to distinguish between the CMEs that correspond to different groups of source structures. In this work, CME-associated long eruptive filaments distributed in three of the four categories according to their background magnetic fields: C1(a), long filaments above the neutral lines of EBRs; C3, transequatorial filaments; and C4, long eruptive filaments along the boundaries of EBRs. The average CME velocities related to long filament eruptions in the 3 categories are 690, 894, and 827 $km{\cdot}s^{-1}$, respectively. Large errors exist in the CME speed estimations because of projection effects, but it is feasible that the CMEs associated with C1(a) are slower than the ones related to the other two categories. Therefore, identifying the possible large-scale source magnetic structure for each CME is only the first step in CME studies. In addition to evaluating the validity of this classification, further efforts need to be made to explore the physical properties of each large-scale

source structure and to understand whether or not the structural characteristics on the solar surface can affect the properties and geo-effectiveness of associated CMEs.

Acknowledgements. We would like to thank Dr. C. J. Xiao for his valuable suggestions. We also thank Mrs Y. Z. Zhang for all her help in extrapolating potential fields. The authors are grateful to the referee for her/his important suggestions and comments, as well as careful corrections of our mistakes. The work is supported by the National Natural Science Foundation of China(G10233050) and the National Key Basic Science Foundation(TG2000078404). We are grateful to all members of the SOHO EIT, LASCO, and MDI teams, as well as the BBSO team, Yohkoh team, HSTRC team, HAFB team, and the HSOS staff who provided the wonderful data. This CME catalog is generated and maintained by NASA and The Catholic University of America in cooperation with the Naval Research Laboratory. SOHO is a project of international cooperation between ESA and NASA.

References

Abramenko, V. I., Wang, T. J. & Yurchishin, V. B. 1996, Sol. Phys., 168, 75
Bao, S. & Zhang, H. 1998, ApJ, 496, L43
Brueckner, G. E. et al. 1995, Sol. Phys., 162, 357
Bumba, V., Garcia, A. & Jordan, S. 1998, A&A, 329, 1138
Canfield, R. C., Pevtsov, A. A., & McClymont, A. N. 1996, in ASP Conf. Ser. Vol. 111, Magnetic Reconnection in the Solar Atmosphere (San Francisco: ASP), 341
Chase, R. C., Krieger, A. S., Svestka, Z., & Vaiana, G. S. 1976, in Space Research XVI, (Berlin : Akademie), 917
Chen, P. F., Shibata, K. 2000, ApJ, 545, 1, 524
Cheng, J. X., Fang, C., Chen, P. F. & Ding, M. D. 2005, Chinese J. Astron. Astrophys., 5, 3, 265
Chertok, I. M. 2001, Sol. Phys., 198, 2, 367
Dere, K. P., Brueckner, G. E., Howard, R. A., Koomen, M. J. & Korendyke, C. M. 1997, Sol. Phys., 175, 601.
Delannée, C., Aulanier, G. 1999, Sol. Phys., 190, 107D
Delannée, C., Delaboudinière, J.-P. & Lamy, P. 2000, A&A, 355, 725
Delaboudinière, J.-P. et al. 1995, Sol. Phys., 162, 291
Domingo, V., Fleck, B., Poland, A. I. 1995, Sol. Phys., 162, 1
Feynman, J., Hundhausen, A. J. 1994, J. Geophys. Res., 99, A5, 8451
Feynman, J., & Martin, S. F. 1995, J. Geophys. Res., 100, 3355
Feynman, J. 1997, in: Nancy Crooker, Joselyn, J. A., Feynman, J.(eds.), Coronal Mass Ejections, Evolving Magnetic Structures and Their Relation to Coronal Mass Ejections (Washington, DC : American Geophysical Union), vol. 99, 299
Forbes, T. G. 2000, J. Geophys. Res., 105(A10), 23153
Gopalswamy, N. & Hanaoka, Y. 1998, ApJ, 498, L179
Gopalswamy, N., Shimojo, M., Lu, W., Yashiro, S., Shibasaki, K. & Howard, R. A. 2003, ApJ, 586, 562
Gosling, J. T. 1997, Coronal mass ejection: an overview, in Coronal Mass Ejections (eds. N. Crooker, J. A. Joselyn, and J. Feynman), AGU Geophysical Monograph 99, 9
Harra, L. K., Matthews, S. A., van Driel-Gesztelyi, L. 2003, ApJ, 598, 59
Harra, L. K., Sterling, A. C. 2003, ApJ, 587, 429
Hundhausen, A. J. 1988, The origin and propagation of coronal mass ejections, Ed. Pizzo, V. J., Holzer, T. E. & Sime, D. G., Proceeding of the Sixth International Solar Wind Conference, NCAR/TN 306+Proc, p181
Hundhausen, A. J. 1997, in Coronal Mass Ejections: Geophysical Monograph 99, ed. Crooker, N. et al. (Washington, DC: AGU), 1
Hundhausen, A. J. 1993, J. Geophys. Res., 98, 13, 177
Hundhausen, A. J., 1999. Coronal Mass Ejections: a summary of SMM observations from 1980 to 1984-1989. In: Strong, K. et al. (Eds.), The Many Faces of the Sun, Springer, New York, pp. 143-200
Khan, J. I., Hudson, H. S. 2000, Geophys. Res. L., 27, 8, 1083
Klimchuk, J. A., Acton, L. W., Harvey, K. L., Hudson, H. S., Kluge, K. L., Sime, D. G., Strong, K. T., Watanabe, Ta. 1994, In: Uchida, Y. et al. (Eds.), X-ray Solar Physics from Yohkoh, Universal Academy Press, Tokyo, pp. 181-186
Lee, J. W. 1992, Sol. Phys., 139, 267
Lin, J. 2004, Sol. Phys., 219, 169
Loughhead, R. E., Wang, J. L. & Blows, G. 1983, ApJ, 274, 883
Maia, D., Voulidas, A., Pick, M., Howard, R., Schwenn, R. & Magalhaes, A. 1999, J. Geophys. Res., 104 (A6), 12, 507
Martin, S. F. 1986, in Coronal and Prominence Plasmas, ed. A. I. Poland (NASA CP-2442; Washington, DC: NASA), 73
McIntosh, P. S. 1980, Solar and Interplanetary Dynamics, Ed. M. Dryer & E. Tandberg-Hanssen, IAU Symp. 91,25
Munro, R. H., et al. 1979, Sol. Phys., 194, 371
Nitta, N. & Akiyama, S. 1999, ApJ, 525, L57
Pevtsov, A. A., Canfield, R. C., & Metcalf, T. R. 1995, ApJ, 440, L109
Pevtsov, A. A. 2000, ApJ, 531, 553
Pevtsov, A. A., Canfield, R. C. & Latushko, S. M. 2001, ApJ, 549, 261
Rust, D. M. & Hildner, E. 1976, Sol. Phys., 48, 381
Scherrer, P. H. et al. 1995, Sol. Phys., 162, 129
Seehafer, N. 1990, Sol. Phys., 125, 219
Shibata, K., et al. 1995, ApJ, 451, L83
Song, L. M., Zhang, J., Yang, Z. L. & Wang, J. X. 2002, Sol. Phys., 211, 315
Sterling A. C., Hudson, H. S. 1997, ApJ, 491, 55
St Cyr, O. C. & Webb, D. F. 1991, Sol. Phys., 136, 379
Subramanian, P., Dere, K. P., Rich, N. B. & IIoward, R. A. 1999, The relationship of coronal mass ejections to streamers. Journal of Geophysical Research 104, 22, 321-22,330
Subramanian, P. & Dere, K. P. 2001, ApJ, 561, 372
Svestka, Z., Krieger, A. S., Chase, R. C., & Howard, R. 1977, Sol. Phys., 52, 69
Tandberg-Hanssen, E. 1995, The Nature of Solar Prominences (Dordrecht: Kluwer)
Thompson, B. J., Plunkett, S. P., Gurman, J. B., Newmark, J. S., St. Cyr, O. C. & Michels, D. J. 1998, Geophys. Res. Letters 25, 2465
Thompson, B. J., Cliver, E. W., Nitta, N., Delannée, C. & Delaboudinière, J.-P. 2000, Geophys. Res. Lett., 27, 1431
Tsuneta, S., et al. 1991, Sol. Phys., 136, 37
Vrabec, D. 1971, in IAU Symp. 43, Solar Magnetic Fields, ed. R. Howard (Dordrecht: Reidel), 329
Wang, T. J., Yan, Y. H., Wang, J. L., Kurokawa, H. & Shibata, K. 2002a, ApJ, 572, 580
Wang, J. & Shi, Z. 1993, Sol. Phys., 143, 119
Wang, J., Li, W. & Denker, C. et al. 2000, ApJ, 530, 1071
Wang, J. 2002b, in 2nd French-Chinese Meeting on Sol. Phys., Understanding active phenomena: progress and perspectives, ed. Henoux, J. C., Fang, C. & Vilmer, N., International Scientific Publishers & World Publishing Corporation press, 145
Wang, J., Zhang, J., Deng, Y. Y., et al. 2002c, Science in China (Series A), 45, L57
Wang, J., Zhou, G. P. & Zhang, J. 2004, ApJ, 615, 1021
Wang, J., Zhou, G. P. & Wen, Y. Y. et al. 2005a, in Proc. IAU Symp. 226, Coronal and Stellar Mass Ejections, ed. Dere, K., Wang, J. X. & Yan, Y. H., Cambridge Univ. Press, 135
Wang, J., Zhou, G. P. & Wen, Y. Y. et al. 2005b, Chinese J. Astron. Astrophys. (acceped)

Wang, Y. -M. & Sheeley Jr, N. R. 1999, ApJ, 510, L157
Webb, D. F., Krieger, A. S. & Rust, D. M. 1976, Sol. Phys., 48, 159
Webb, D. F. & Hundhausen, A. J. 1987, Sol. Phys., 108, 383
Webb D. F. 2000, J. of Atmospheric and solar-terrestrial phys., 62, 1415
Wills-Davey, M. J. & Thompson, B. J. 1999, Sol. Phys. 190, 459
Zhang, J., Dere, K. P. & Howard, R. A., et al. 2001a, ApJ, 559, 452
Zhang, J. & Wang, J. X. 2000, Geophys. Res. Lett., 27, 18, 2877
Zhang, J., Wang, J. X. & Nitta, N. 2001b, Chinese J. Astron. Astrophys., 1, 85
Zhang, J., Wang, J. X. & Deng, Y. Y., et al. 2001c, ApJ, 548, L99
Zhang, J. & Wang, J. X. 2002, ApJ, 566, L117
Zhou, G. P., Wang, J. X. & Cao, Z. L. 2003, A&A, 397, 1057
Zhou, G. P., Wang, Y. M. & Wang, J. 2005, Adv. Space Res. (in press)
Zirin, H., 1985, Australian J. Phys. 36, 961

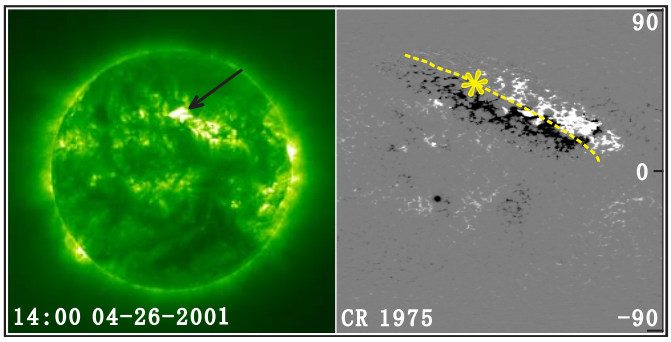

Fig. 1. Allocating a CME associated surface activity in the corresponding MDI synoptic chart according to its position in EIT images. The surface activity is indicated by a black arrow in the left EIT image, and its position is shown by a asterisk on the right MDI synoptic chart. The right panel also indicates the definition of an extended magnetic bipole in the MDI synoptic chart; the dashed line denotes the magnetic neutral line of the EBR.

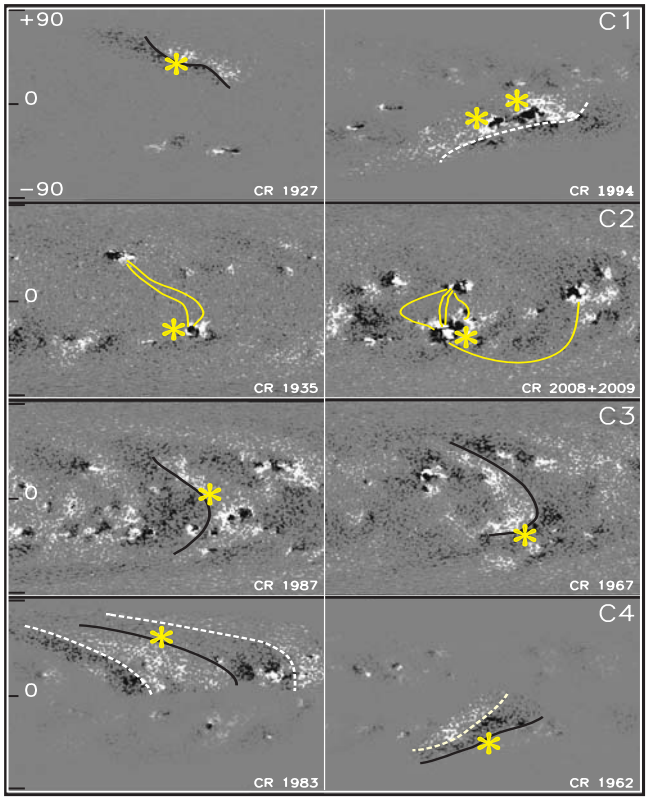

Fig. 2. The four categories identified for CME large-scale source structures shown on MDI synoptic charts; from top to bottom row: Category One (C1), extended bipolar regions (EBRs); Category Two (C2), transequatorial magnetic loops; Category Three (C3), transequatorial filaments and their background magnetic fields; and Category four (C4), long filaments along the boundary of EBRs. In this figure, the asterisks indicate the positions of CME-associated surface activity; the black solid lines in the graph denote filaments; the white dash lines show the magnetic neutral lines of EBRs; the light solid lines indicate transequatorial loops. The scale of each panel in this figure in latitude and longitude is 180°×180°

.

Online Material

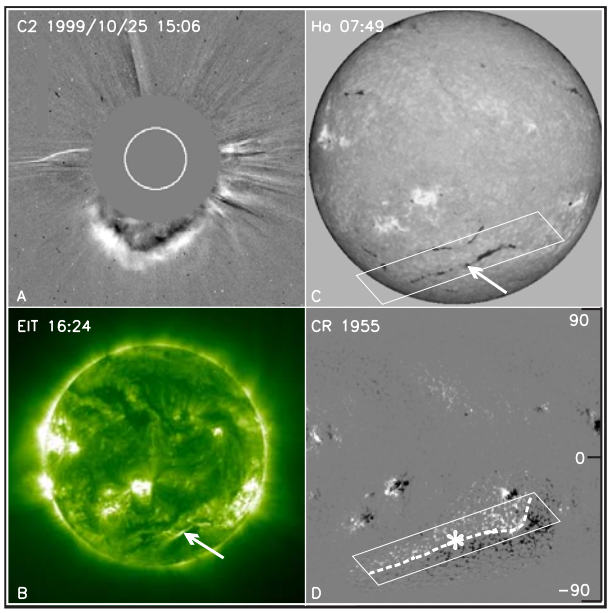

Fig. 3. An example of a CME correlated with the eruption of a filament in an EBR: A, LASCO C2 image; B, EIT image showing the post-flare loop after the filament eruption indicated by an arrow; C, Hα image; D, subset of the MDI synoptic chart in CR 1955. The CME-associated surface activity (represented by the asterisk) took place in an EBR; the EBR is shown more clearly by a procedure that artificially weakens the other surrounding magnetic features. The dashed line indicates the EBR neutral line; quadrangles in Panels C and D denote the position of the eruptive filament in an Hα image and on the corresponding MDI synoptic chart.

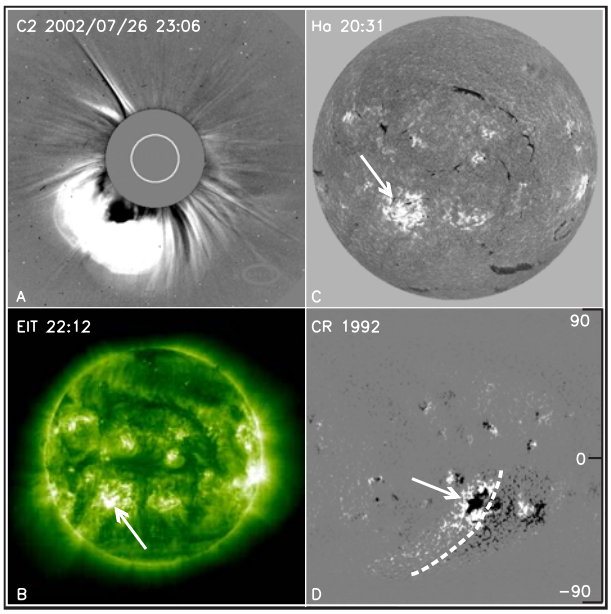

Fig. 4. A CME on Jul. 26, 2002 whose correlated surface activity appeared in a complex active region (AR) inside an EBR. The propagating CME is shown in Panel A, a LASCO C2 image; its associated flare is indicated by an arrow in Panel B, an EIT image. From panel C, an Hα image, the eruptive AR filament can be seen. Panel D is a part of the MDI synoptic chart in CR 1992 with the scale of 180°×180° in latitude and longitude, and shows the associated EBR; the dashed line indicates the EBR's magnetic neutral line; three arrows in the figure denote the CME-associated surface activity in different observations.

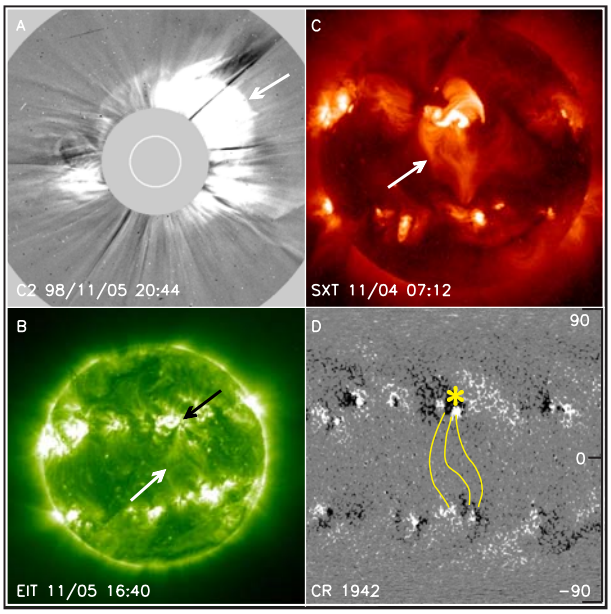

Fig. 5. Identifying a CME on Nov. 5, 1998 associated with transequatorial loops. The CME propagated northward seen from a LASCO C2 image of Panel A. Its related preexisting transequatorial loops are indicated by white arrows in Panels B and C, an EIT image and an SXT image. Based on the magnetic loop morphologies in the EIT image, the transequatorial loops are mapped on the corresponding MDI synoptic chart in CR 1942, represented by light solid lines in panel D. The transequatorial loops connect a complex AR in the northern hemispheres with a plage region in the southern hemisphere; the asterisk indicates the location of the CME-related surface activity. The scale of the subset of synoptic chart is 180°×180° in latitude and longitude.

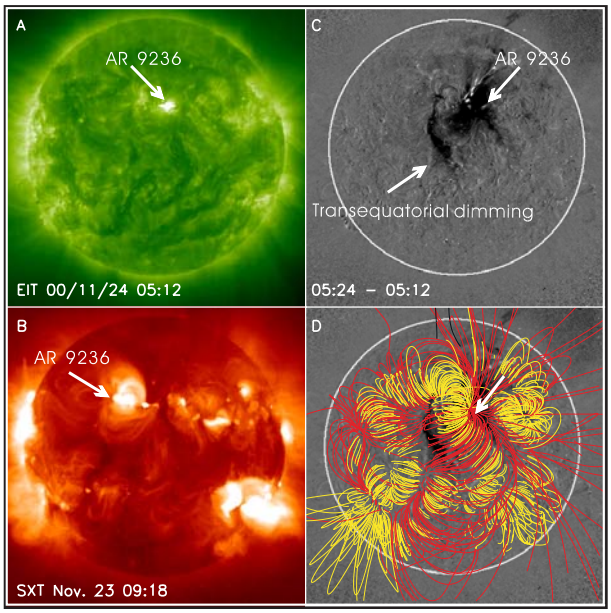

Fig. 6. An example on Nov. 24, 2000 is presented to explain that CME-associated transequatorial loop is manifested by transequatorial dimming. From Panels A and B, EIT and SXT images, we cannot easily observe the associated transequatorial loop. Arrows in these two panels show the CME-associated surface activity. Panel C: transequatorial dimming (indicated by an arrow) is linked to transequatorial loops. Panel D: based on a potential extrapolation of 3-dimension magnetic lines of force, transequatorial magnetic lines (see the arrow) are shown to overlay the dimming regions.

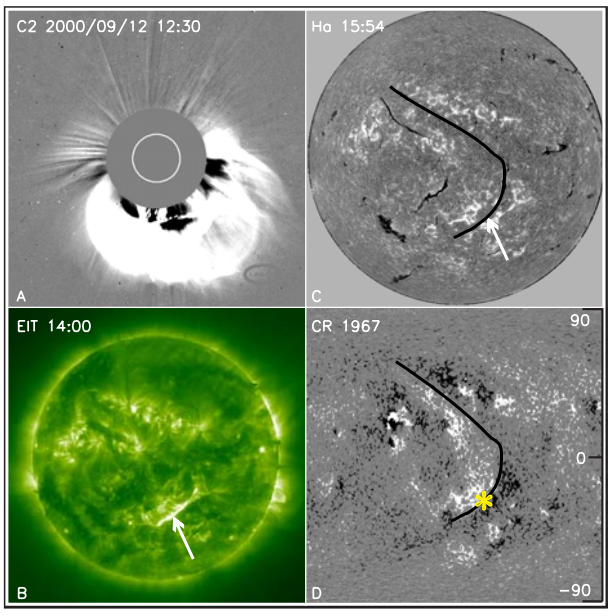

Fig. 7. A CME related to a transequatorial filament eruption. Panel A is a LASCO C2 image showing the CME propagating southwestward. After the eruption of the transequatorial filament, post-flare loops can be seen in an EIT image of Panel B, denoted by an arrow. The transequatorial filament is indicated by a arrow and highlighted by a black line in an Hα image from BBSO in Panel C. A subset of MDI synoptic chart in CR 1967 in Panel D shows the background magnetic field of the filament, the solid line represents the filament, the asterisk symbol denotes the position of the CME-associated surface activity, the scale of the synoptic chart also is 180°×180° in latitude and longitude.

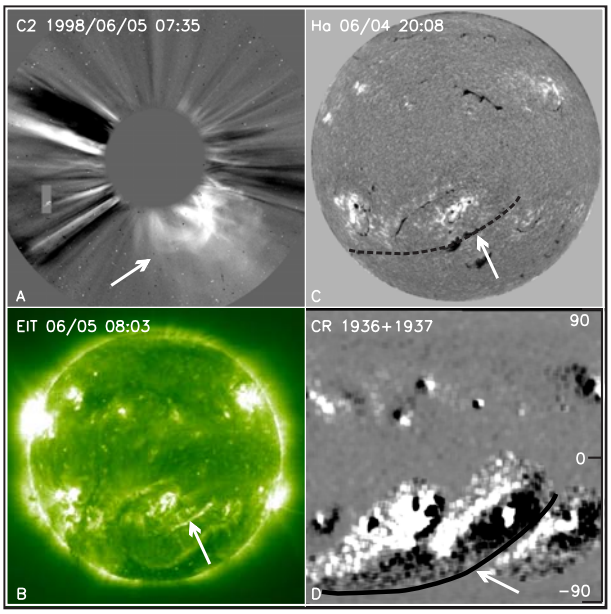

Fig. 8. An example illustrates CMEs associated with long filament eruptions along boundary of EBRs. A CME on Jun. 5, 1998 is shown in a LASCO C2 image of Panel A indicated by an arrow. Post-flare loops formed after the filament eruption in an EIT image of Panel B, denoted by an arrow. The eruptive filament is highlighted by a black dashed line in Panel C, an Hα image in its pre-eruption stage. From the corresponding subset of the MDI synoptic chart of Panel D, the long eruptive filament is found on the boundary of three EBRs, shown by a black line and denoted by an arrow. The scale of the subset of synoptic chart is 180°×180° in latitude and longitude.

Appendix

Table A1: List of all the 288 sampling CMEs and their large-scale magnetic structures

Category	No.	Date	TM[a] (UT)	CPA[b]	Width[c]	Speed[d] (km·s^{-1})	Position[e]	NOAA[f]	AR (y/n)
C1(a)	1	1997-8-30	1:30	halo	360	371	N32E11		y
	2	1997-9-28	1:08	halo	360	359	N35E10		n
	3	1997-10-6	15:28	139	174	293	S60E20		y
	4	1997-10-21	18:03	halo	360	523	N17E05	8097	y
	5	1998-1-2	23:28	halo	360	438	N24W42		y
	6	1998-1-17	4:09	halo	360	350	S41E17		n
	7	1998-1-21	6:37	halo	360	361	S49E10		n
	8	1998-1-25	15:26	halo	360	693	N24E25		n
	9	1998-6-8	16:27	177	240	433	N35E51		n
	10	1998-12-18	18:09	halo	360	1749	N30E37	8414	y
	11	1999-3-21	15:26	208	139	398	S28W12		n
	12	1999-4-17	6:36	213	165	362	S21W10		n
	13	1999-6-14	12:50	129	148	560	S85E0		n
	14	1999-6-24	13:31	halo	360	975	N31W09	8595	y
	15	1999-7-16	20:30	291	131	462	N35W60		n
	16	1999-8-17	13:31	61	261	776	N22E34	8668	y
	17	1999-9-3	0:06	184	175	512	S39W27		y
	18	1999-9-20	6:06	halo	360	604	S18E01		y
	19	1999-10-25	14:26	186	146	511	S38W12		n
	20	2000-2-9	19:54	halo	360	910	S14W40	8853	y
	21	2000-6-6	15:54	halo	360	1119	N21E16	9026	y
	22	2000-6-7	16:30	halo	360	842	N23E03	9026	y
	23	2000-6-10	17:08	halo	360	1108	N22W38	9026	y
	24	2000-6-27	10:54	349	132	811	N42W53		n
	25	2000-11-1	16:26	halo	360	801	S14E37	9214	y
	26	2001-1-24	8:54	249	196	536	S28W12	9323	y
	27	2001-2-11	1:30	halo	360	1183	N24W57	9346	y
	28	2001-3-19	5:26	halo	360	389	S20W01		n
	29	2001-4-14	21:30	151	132	764	S20W06		n
	30	2001-4-26	12:30	halo	360	1006	N23W05	9433	y
	31	2001-5-25	17:26	90	208	930	S13E90		n
	32	2001-8-19	6:06	halo	360	556	N30W75		n
	33	2002-2-20	6:30	Halo	360	952	N20W70	9824	y
	34	2002-4-8	8:06	209	>158	251	S25W05	9900	y
	35	2002-10-25	18:06	336	132	1030	N30W10		n
	36	2002-12-12	2:30	99	146	187	S15E30	10218	y
	37	2002-12-21	2:30	2	225	1072	N45E10	10229	y
	38	2002-12-22	3:30	328	272	1071	N27W46	10225	y
	39	2003-1-7	8:30	128	131	365	S22E25	10244	y
	40	2003-3-3	21:08	114	201	702	S22E65		y
	41	2003-3-14	18:06	232	137	991	S17W50		n
C1(b)	1	1999-5-11	22:26	86	193	735	S21E80		y
	2	1999-5-27	14:50	66	140	646	N22E68		y
	3	1999-6-4	7:26	289	150	2230	N19W75	8552	y
	4	1999-6-10	5:26	351	131	434	N31W12		y
	5	1999-6-12	21:26	halo	360	465	N24W34	8574	y
	6	1999-6-22	18:54	halo	360	1133	N23E40		y
	7	1999-6-28	21:30	halo	360	1083	N26W42	8592	y
	8	1999-7-19	3:06	halo	360	430	N15W14		y
	9	1999-8-7	23:50	169	185	283	S28E03	8657	y
	10	1999-9-13	9:30	0	182	898	N22E10	8699	y
	11	1999-9-13	17:31	109	184	444	N16W03	8693	y
	12	1999-10-14	9:26	halo	360	1250	N12E37	8731	y
	13	1999-12-6	9:30	halo	360	653	N07E44		y

Table A1 continued

Category	No.	Date	TM[a] (UT)	CPA[b]	Width[c]	Speed[d] (km·s^{-1})	Position[e]	NOAA[f]	AR (y/n)
	14	1999-12-22	2:30	halo	360	570	N30E30	8806	y
	15	2000-1-28	20:12	halo	360	429	S31W17	8841	y
	16	2000-4-10	0:30	halo	360	409	S14E01	8948	y
	17	2000-5-10	20:06	83	205	641	N14E20	8990	y
	18	2000-6-25	7:54	262	165	1617	N16W55	9046	y
	19	2000-6-28	19:31	270	134	1198	N24W85	9051	y
	20	2000-9-15	12:06	249	235	633	N13E08	9165	y
	31	2000-9-15	15:26	halo	360	481	N12E07	9165	y
	22	2000-9-16	5:18	halo	360	1215	N14W07	9165	y
	23	2000-10-2	3:50	halo	360	525	S09E07	9176	y
	24	2000-10-2	20:26	halo	360	569	S10W02	9176	y
	25	2000-11-23	21:30	124	148	1198	S32E62	9239	y
	26	2001-2-3	0:30	86	203	639	N09E72	9334	y
	27	2001-2-5	15:54	74	136	474	N07E38	9335	y
	28	2001-6-22	12:54	269	270	638	S26W51	9509	y
	29	2001-8-25	16:50	halo	360	1433	S17E34	9591	y
	30	2001-8-28	16:27	105	148	478	N16E70	9600	y
	31	2001-9-11	14:54	halo	360	791	N14E34	9615	y
	32	2001-9-17	8:54	198	166	1009	S14E04	9616	y
	33	2001-9-22	9:42	283	134	364	N27W8	9626	y
	34	2001-9-24	10:31	halo	360	2402	S16E25	9632	y
	35	2001-9-28	8:55	halo	360	846	N10E18	9636	y
	36	2001-9-28	10:31	198	136	665	S18W36	9628	y
	37	2001-9-29	11:54	114	216	509	N13E03	9636	y
	38	2001-10-22	15:06	halo	360	1336	S20E18	9672	y
	39	2001-11-10	13:27	85	155	480	N15E85	9695	y
	40	2001-11-15	20:50	32	164	618	N22E0	9703	y
	41	2001-11-22	20:31	halo	360	1443	S25W67	9698	y
	42	2001-11-28	17:30	halo	142	500	N04E15	9715	y
	43	2001-12-11	8:30	23	142	804	N16E41	9733	y
	44	2001-12-13	14:54	halo	360	864	N16E09	9733	y
	45	2001-12-26	5:12	halo	360	1446	N08W54	9742	y
	46	2002-4-4	5:06	108	133	468	S14E55	9906	y
	47	2002-4-10	13:27	340	159	650	N30E02	9901	y
	48	2002-4-15	3:50	Halo	360	720	S05W05	9906	y
	49	2002-5-7	4:06	Halo	360	720	S02E28	9927	y
	50	2002-7-26	22:06	Halo	360	818	S22E22	10039	y
	51	2002-9-16	3:54	236	133	256	S15W35	10105	y
	52	2002-9-17	2:30	104	147	681	N20W75	10110	y
	53	2002-9-17	8:06	210	249	960	S15W36	10114	y
	54	2002-9-19	5:54	120	169	621	S10E75	10125	y
	55	2002-10-3	3:54	144	132	834	S20E10	10137	y
	56	2002-11-3	17:30	281	151	982	N15E24	10177	y
	57	2002-11-9	13:31	Halo	360	1838	S10W30	10182	y
	58	2002-11-10	3:30	203	282	1670	S15W40	10182	y
	59	2002-12-10	6:06	114	164	175	S12E50	10220	y
	60	2003-2-16	23:08	279	151	603	N20W85	10282	y
	61	2003-6-15	14:30	96	140	937	S10E85	10386	y
	62	2003-6-17	23:18	Halo	360	1813	S08E60	10386	y
	63	2003-11-11	13:54	Halo	360	1315	S03W65	10498	y
C2	1	1997-3-9	4:30	54	146	517	N03E75		y
	2	1997-4-7	14:27	halo	360	878	S25E16	8027	y
	3	1997-9-23	22:02	133	155	712	S31E26		y
	4	1997-11-4	6:10	halo	360	785	S18W30		y

Table A1 continued

Category	No.	Date	TM[a] (UT)	CPA[b]	Width[c]	Speed[d] (km·s^{-1})	Position[e]	NOAA[f]	AR (y/n)
	5	1997-11-6	12:10	halo	360	1556	S18W63		y
	6	1998-4-27	8:56	halo	360	1385	S18E50	8210	y
	7	1998-4-29	16:58	halo	360	1374	S15E19	8210	y
	8	1998-5-1	23:40	halo	360	585	S19W05	8210	y
	9	1998-5-2	5:31	halo	360	542	S19W10	8210	y
	10	1998-5-2	14:06	halo	360	938	S15W15	8210	y
	11	1998-5-3	22:02	317	194	649	S12W33	8214	y
	12	1998-5-6	8:29	309	190	1099	S11W66	8210	y
	13	1998-5-27	13:45	175	268	878	N17W62		y
	14	1998-11-2	14:18	116	169	661	S25E47		y
	15	1998-11-4	7:54	halo	360	523	N17W01	8375	y
	16	1998-11-5	2:02	halo	360	380	N13W16		y
	17	1998-11-5	20:44	halo	360	1118	N22W18		y
	18	1999-4-13	3:30	halo	360	291	N20E02		n
	19	1999-5-10	5:50	halo	360	920	N16E19	8539	y
	20	1999-6-29	18:54	halo	360	438	N19E00		y
	21	1999-7-28	5:30	halo	360	457	S14E05		y
	22	1999-7-28	9:06	halo	360	462	S14E03		y
	23	1999-8-2	7:26	99	189	286	N14E25		y
	24	1999-8-2	22:26	271	157	292	S18W46	8647	y
	25	1999-8-4	6:26	262	144	405	S18W62	8647	y
	26	1999-8-28	18:26	120	245	462	S26W14	8674	y
	27	1999-9-1	2:30	188	283	253	N08W08	8677	y
	28	2000-1-18	17:54	halo	360	739	S19E11	8831	y
	29	2000-2-8	9:30	halo	360	1079	N25E26	8858	y
	30	2000-2-11	13:31	halo	360	521	S13W22	8856	y
	31	2000-2-12	4:31	halo	360	1107	N26W23	8858	y
	32	2000-2-17	20:06	halo	360	682	S25W16	8869	y
	33	2000-5-15	16:26	257	165	1212	S24W67	8993	y
	34	2000-7-23	5:30	161	181	631	S10W10	9091	y
	35	2000-7-25	3:30	halo	360	528	N06W08	9097	y
	36	2000-9-1	6:30	261	142	427	S20W18	9143	y
	37	2000-9-6	16:30	224	144	500	S20W19	9145	y
	38	2000-9-7	21:30	297	169	422	N06W47	9151	y
	39	2000-9-25	2:50	halo	360	587	N08W20	9167	y
	40	2000-10-26	16:50	114	145	359	S20E64	9209	y
	41	2000-11-23	6:06	halo	360	492	S26W40	9238	y
	42	2000-11-24	5:30	halo	360	994	N23W05	9236	y
	43	2000-11-24	15:30	halo	360	1245	N22W07	9236	y
	44	2000-11-24	22:06	halo	360	1005	N21W14	9236	y
	45	2000-11-25	1:31	halo	360	2519	N07E50	9240	y
	46	2000-11-25	9:30	halo	360	675	N18W24	9236	y
	47	2000-11-25	19:31	halo	360	671	N20W23	9236	y
	48	2000-11-26	17:06	halo	360	980	N18W38	9236	y
	49	2001-1-10	0:54	halo	360	832	N13E36	9306	y
	50	2001-1-28	15:54	247	250	916	S04W59	9313	y
	51	2001-1-29	16:06	149	261	651	S09E57	9329	y
	52	2001-3-20	3:26	270	199	478	S10W35	9380	y
	53	2001-3-24	20:50	halo	360	906	N15E22	9390	y
	54	2001-3-25	17:06	halo	360	677	N16E25	9402	y
	55	2001-3-28	12:50	halo	360	519	N18E02	9393	y
	56	2001-3-29	10:26	halo	360	942	N20W19	9393	y
	57	2001-4-5	17:06	halo	360	1390	S24E50	9415	y
	58	2001-4-6	19:30	halo	360	1270	S21E31	9415	y
	59	2001-4-9	0:06	159	221	653	S15E10	9415	y
	60	2001-4-9	15:54	halo	360	1192	S21W04	9415	y

Table A1 continued

Category	No.	Date	TM[a] (UT)	CPA[b]	Width[c]	Speed[d] (km·s^{-1})	Position[e]	NOAA[f]	AR (y/n)
	61	2001-4-10	5:30	halo	360	2411	S23W09	9415	y
	62	2001-4-11	13:32	halo	360	1103	S22W27	9415	y
	63	2001-4-12	10:31	halo	360	1184	S15W35	9415	y
	64	2001-4-14	17:54	239	190	830	S16W71	9415	y
	65	2001-4-15	14:06	245	167	1199	S21W85	9415	y
	66	2001-7-19	10:30	275	166	1668	S8W62	9537	y
	67	2001-10-3	2:54	163	152	389	E09S19	9641	y
	68	2001-10-19	1:27	267	254	558	N16W18	9661	y
	69	2001-10-19	16:50	halo	360	901	N15W29	9661	y
	70	2001-10-24	6:26	62	145	597	S15E30	9675	y
	71	2001-10-25	15:26	140	141	1092	S16W21	9672	y
	72	2001-11-1	22:30	halo	360	453	N12W23	9682	y
	73	2001-11-22	23:30	halo	360	1437	S17W36	9704	y
	74	2002-3-15	23:06	Halo	360	957	S08W03	9866	y
	75	2002-5-8	13:50	Halo	360	614	S12W07	9934	y
	76	2002-7-1	13:31	160	135	882	S19E60	10019	y
	77	2002-7-15	20:30	Halo	360	1151	N20E05	10030	y
	78	2002-7-15	21:30	14	>188	1300	N20E02	10030	y
	79	2002-7-17	7:31	36	177	716	N21W17	10030	y
	80	2002-7-29	12:07	332	154	562	N10W22	10039	y
	81	2002-7-29	23:30	351	130	360	S10W06	10050	y
	82	2002-8-14	2:30	297	133	1309	N09W54	10061	y
	83	2002-8-16	12:30	Halo	360	1585	S14E20	10069	y
	84	2002-8-18	21:54	203	140	682	S12W19	10069	y
	85	2002-8-20	1:54	244	>157	961	S13W36	10069	y
	86	2002-8-22	2:06	Halo	360	998	S07W62	10069	y
	87	2002-8-23	6:26	103	134	496	S11E23	10085	y
	88	2002-8-23	8:50	106	143	999	S08E72	10087	y
	89	2002-8-23	20:50	262	131	861	S17W15	10087	y
	90	2003-3-18	12:30	263	209	1601	S09W46	10314	y
	91	2003-3-18	13:54	Halo	360	1042	S09W46	10314	y
	92	2003-4-23	1:27	271	248	916	N22W25	10338	y
	93	2003-4-24	13:27	317	242	609	N21W39	10338	y
	94	2003-7-4	15:30	81	174	751	N05E30	10400	y
	95	2003-7-17	8:54	141	>298	531	N14E13	10412	y
	96	2003-8-14	20:06	Halo	360	378	N08E25	10067	y
	97	2003-10-19	17:08	34	150	472	N08E58	10484	y
	98	2003-10-22	8:30	286	>267	719	N04E20	10484	y
	99	2003-10-22	20:06	93	134	1085	S15E85	10486	y
	100	2003-10-23	8:54	53	>236	1406	S21E88	10486	y
	101	2003-10-26	6:54	108	>207	1371	S15E44	10486	y
	102	2003-10-26	17:54	270	>171	1537	N02W38	10484	y
	103	2003-10-27	8:30	265	144	1322	N00W45	10484	y
	104	2003-10-28	10:54	124	147	1054	S19E16	10486	y
	105	2003-10-28	11:30	Halo	360	2459	S16E08	10486	y
	106	2003-10-29	20:54	Halo	360	2029	S15W02	10486	y
	107	2003-11-1	21:30	318	>143	413	N06W55	10488	y
	108	2003-11-2	9:30	Halo	360	2036	S20W90	10486	y
	109	2003-11-2	17:30	Halo	360	2598	S14W56	10486	y
	110	2003-11-13	9:30	49	217	1141	N04E87	10501	y
	111	2003-11-17	9:26	72	>242	1061	N00E32	10501	y
	112	2003-11-18	8:50	Halo	360	1660	N00E18	10501	y
	113	2003-11-18	9:50	95	>197	1824	N01E19	10501	y
	114	2003-11-20	8:06	Halo	360	669	N03W09	10501	y

Table A1 continued

Category	No.	Date	TM[a] (UT)	CPA[b]	Width[c]	Speed[d] (km·s^{-1})	Position[e]	NOAA[f]	AR (y/n)
	115	2003-12-2[2]	10:50	261	>150	1393	S12W90	10511	y
	116	2003-12-25[2]	2:30	198	>201	519	S11E03	10532	y
C3	1	2000-7-14	10:54	halo	360	1674	N22W07	9077	y
	2	2000-8-9	16:30	halo	360	702	N20E12	9114	y
	3	2000-9-5	5:54	3	138	473	N22E10		n
	4	2000-9-12	11:54	halo	360	1550	S17W09		n
	5	2000-11-8	23:06	halo	360	1738	N14W63	9213	y
	6	2000-11-26	3:30	259	188	495	S25W50		n
	7	2000-12-14	17:06	halo	360	725	N18E04	9267	y
	8	2001-1-20	19:32	halo	360	839	S07E40	9313	y
	9	2001-1-20	21:30	halo	360	1507	S07E46	9313	y
	10	2001-1-26	1:54	275	148	648	N30W69		n
	11	2001-1-26	12:06	276	176	928	S24W60	9320	y
	12	2001-2-15	13:54	halo	360	625	N08E10		n
	13	2001-5-21	23:06	254	160	364	N05W12		n
	14	2001-6-5	5:06	117	150	836	S18E44	9488	y
	15	2001-8-9	10:30	285	175	479	N10W15		n
	16	2001-9-9	14:54	98	143	967	E70S24		y
	17	2001-11-17	5:30	halo	360	1379	S13E42	9704	y
	18	2001-11-21	14:06	halo	360	518	n40e08	9704	y
	19	2002-3-17	10:34	182	187	989	N0W10		n
	20	2002-3-17	20:06	184	153	823	N00W05		n
	21	2002-3-18	2:54	Halo	360	989	N00W15		n
	22	2002-3-19	9:54	232	134	722	S05W45	9866	y
	23	2002-3-20	23:54	242	>160	1075	S10W17	9871	y
	24	2002-4-17	8:26	Halo	360	1240	S04W37	9906	y
	25	2002-4-21	1:27	Halo	360	2393	S14W84	9906	y
	26	2002-6-19	3:54	70	151	436	N24E60	10005	y
	27	2002-8-1	4:06	212	139	375	S15E10	10057	y
	28	2002-8-6	18:25	218	134	1098	S35W30		n
	29	2002-11-24	20:30	Halo	360	1077	N20E35		n
	30	2002-12-19	22:06	Halo	360	1092	N22W12	10225	y
	31	2003-1-20	21:30	58	166	555	N28E50		n
	32	2003-1-23	23:30	105	138	350	S10W06		n
	33	2003-1-27	22:23	205	267	1053	S15W18		n
	34	2003-1-30	10:06	2	138	620	N26E00		n
	35	2003-4-4	21:50	298	158	250	S08W43	10324	y
	36	2003-4-25	5:50	81	235	806	N18E76	10346	
	37	2003-4-26	21:50	48	166	672	N13E65		n
C4	1	1998-4-20	10:07	284	165	1863	S47W70		n
	2	1998-6-5	7:02	205	132	1017	S29W17		y
	3	1998-6-5	12:01	halo	360	320	S26W27		n
	4	1998-11-5	2:41	155	180	568	S30E10		y
	5	1998-11-9	18:17	330	190	325	N20W02		y
	6	1999-5-3	6:06	halo	360	1584	N22E46		y
	7	1999-7-27	1:31	50	193	768	N28E80		y
	8	1999-8-9	3:26	197	212	395	S29W11		y
	9	1999-9-16	16:54	6	147	1021	N42W30		n
	10	1999-11-26	17:30	228	145	409	S40E02		n
	11	2000-4-4	16:32	halo	360	1188	N16W66	8933	y
	12	2000-5-8	14:26	216	137	465	S29W14		n
	13	2000-7-10	21:50	67	360	1352	N45E60		n
	14	2000-8-3	8:30	302	218	896	N23W60		n
	15	2000-8-29	7:54	232	157	516	S58W50		n
	16	2000-9-4	6:06	327	145	849	N27W30		n
	17	2000-10-9	23:50	halo	360	798	N01W14	9182	y
	18	2000-12-18	11:50	halo	360	510	N15E01	9269	y

Table A1 continued

Category	No.	Date	TM[a] (UT)	CPA[b]	Width[c]	Speed[d] (km·s^{-1})	Position[e]	NOAA[f]	AR (y/n)
	19	2001-1-14	6:30	327	134	945	N60W10		n
	20	2001-2-10	5:54	halo	360	956	N37W03		n
	21	2001-3-11	5:50	230	165	404	S55W70		n
	22	2001-7-12	0:06	240	148	736	S45W70		n
	23	2001-10-28	0:26	85	200	592	N40E80		n
	24	2002-1-4	9:30	Halo	360	896	N30E75		n
	25	2002-2-14	2:30	204	>137	473	S25W18		n
	26	2002-3-2	15:06	124	149	1131	S30E80		n
	27	2002-9-5	16:54	Halo	360	1748	N08E29		n
	28	2002-10-2	7:31	170	190	903	S48E05		n
	29	2002-10-15	12:54	193	172	842	S40E10		n
	30	2002-10-25	10:06	Halo	360	629	S30E50		n
	31	2002-11-14	0:06	121	182	542	S50E50	10191	y
	Total	earth-directed	halo	CMEs			288		

* C1,C2,C3 and C4 denote the categories of the CME large-scale structures described in the text;
C1(a)– CMEs associated with long eruptive filaments in EBRs ,
C1(b)– CMEs related to AR activity in EBRs;
[a] CME first appeared in LASCO C2 observations;
[b] the central position angle of a CME;
[c] CME span angle;
[d] CME linear fit speed;
[e] positions of CME-associated surface activity in the disc;
[f] one of CME associated AR numbers;